Predicting magnetic anisotropy energies using site-specific spin-orbit coupling energies and machine learning: Application to iron-cobalt nitrides

Timothy Liao , 1,2,* Weiyi Xia , 3,† Masahiro Sakurai , 1,4 Renhai Wang , 3,5 Chao Zhang , 6 Huaijun Sun, 3,7 Kai-Ming Ho, ^{3,8} Cai-Zhuang Wang, ^{3,8} and James R. Chelikowsky ^{6,2}, ¹Center for Computational Materials, Oden Institute for Computational Engineering and Sciences, The University of Texas at Austin, Austin, Texas 78712, USA ²Department of Physics, The University of Texas at Austin, Austin, Texas 78712, USA ³Department of Physics and Astronomy, Iowa State University, Ames, Iowa 50011, USA ⁴The Institute for Solid State Physics, The University of Tokyo, Kashiwa, Chiba 277-8581, Japan ⁵School of Physics and Optoelectronic Engineering, Guangdong University of Technology, Guangzhou 510006, China ⁶Department of Physics, Yantai University, Yantai 264005, China ⁷ Jiyang College of Zhejiang Agriculture and Forestry University, Zhuji 311800, China ⁸Ames Laboratory, U.S. Department of Energy, Ames, Iowa 50011, USA ⁹McKetta Department of Chemical Engineering, The University of Texas at Austin, Austin, Texas 78712, USA



(Received 18 October 2021; revised 21 December 2021; accepted 19 January 2022; published 7 February 2022)

We present a promising machine-learning model, which focuses on site magnetic properties for rapid screening in materials design. We perform high-throughput first-principles calculations to predict the magnetic anisotropy energies of a variety of iron-cobalt nitrides. We illustrate the efficacy of a spatial decomposition technique that divides the total magnetic anisotropy energy into contributions from individual sites in terms of spin-orbit coupling energies. The spatial decomposition scheme that we utilized works for a wide range of magnetic anisotropy energies. We also construct a machine-learning model by combining the site-specific spin-orbit coupling energies with structural details on each atomic site. We adopt the same approach to predicting the site-specific magnetic moments. We demonstrate the capability of our machine-learning model to accelerate computational screening of candidate materials that possess high magnetizations and large magnetic anisotropy energies.

DOI: 10.1103/PhysRevMaterials.6.024402

I. INTRODUCTION

Magnetocrystalline anisotropy is a basic magnetic phenomenon arising from spin-orbit interactions [1,2]. Such interactions reflect a relativistic effect, which couples electron spin and orbital angular momentum and results in magnetic moments aligning in a specific direction. There is growing interest in the magnitude of magnetic anisotropy [3]. An increase in the strength of uniaxial magnetic anisotropy can lead to higher coercivity, making it possible to enhance the maximum energy product, a standard measure for the performance of a permanent magnet. The maximum energy product is defined as the maximum of the product of Band H in the second quadrant of the B-H curve, where $B = \mu_0(H + M)$ is the flux density and μ_0 is the magnetic permeability in vacuum. In addition to uniaxial magnetic anisotropy, magnetic anisotropy in chiral magnets can be a key parameter for a helical magnetic ordering [4] called "skyrmions."

Common permanent magnets are composed using rareearth and transition-metal elements, such as Nd-Fe-B and Sm-Co [5,6]. The f electrons of rare earths play an important role in enhancing the magnetic anisotropy in rare-earth magnets. Magnets for recording-media applications often contain expensive metals, such as Pt, to control magnetic anisotropy [7,8]. These elements are considered as "critical" resources [9,10] owing to concerns about production and availability of these elements. For these reasons, efforts have been made to discover new magnetic materials without relying on rare earths or expensive metals [11,12].

For example, recent work integrating computational and nonequilibrium fabrication methods has led to the discovery of new rare-earth-free magnetic materials with a noncubic symmetry (e.g., a tetragonal or hexagonal structure) [12]. These magnet materials include FeCo-based alloys [13–19] and ZrCo-based alloys [20-23]. Doping of a light nontoxic element, such as boron and nitrogen, is a common strategy to stabilize the Fe-rich noncubic structures.

Recently, various machine-learning (ML) techniques and data science have been adopted as efficient tools to understand and predict the crystal structures and physical phenomena [24–28]. Notably, a combination of ML methods with highthroughput first-principles calculations enables one to build an automated framework for designing new magnetic materials [29,30]. Recent effort in this research area includes the construction of open-access materials databases and data-sharing platforms [31-37]. In particular, the Magnetic Materials Database [32] is specialized for the magnetic properties of

^{*}timothy.liao@utexas.edu

[†]weiyixia@iastate.edu

rare-earth-free magnets, with an emphasis on site-specific data, such as the local magnetic moment for each atomic site. These site-specific quantities are suitable as training data for machine-learning and data-mining approaches.

Our goal in this study is to build a ML model focusing on site-specific spin-orbit anisotropy energy. The layout of the remainder of the paper is as follows. In Sec. II, we detail the settings for our first-principles calculations and construct a machine-learning model by combining the calculated site-specific magnetic properties with structural details for each site. In Sec. III, we describe the origin of the variety of iron-cobalt nitrides that were used. In Sec. IV, we demonstrate the efficacy of a spatial decomposition scheme and illustrate the capability of our machine-learning model to facilitate computational screening of candidate materials with high magnetization and large magnetic anisotropy energies. We summarize this work in Sec. V.

II. THEORY

A. First-principles calculations

Our first-principles calculations are based on density-functional theory (DFT) [38,39]. We adopt the generalized gradient approximation (GGA) of Perdew, Burke, and Ernzerhof (PBE) [40] for the exchange-correlation energy functional. We use the projector-augmented wave (PAW) method [41] with a cutoff energy of 500 eV. The Monkhorst-Pack scheme [42] is used to generate a k-point grid with a mesh size of $2\pi \times 0.025 \text{ Å}^{-1}$. This mesh size is fine enough to sample the first Brillouin zone for achieving k-point convergence [43]. All DFT calculations are performed using Vienna *ab initio* simulation package (VASP) [44,45].

We perform spin-polarized calculations for collinear magnetism in a self-consistent manner. We then include the spin-orbit couplings and perform a non-self-consistent calculation [46]. When the spin-orbit couplings are included, symmetry operations are omitted, and the spin-quantization axis is set to the chosen direction.

B. Formation energy

The formation energy per atom, $E_{\rm f}$, of an ${\rm Fe}_{\alpha}{\rm Co}_{\beta}{\rm N}_{\gamma}$ structure with $\alpha+\beta+\gamma=1$ is calculated with respect to a linear combination of the total energies per atom of reference elemental phases:

$$E_{\rm f} = E(\text{Fe}_{\alpha}\text{Co}_{\beta}\text{N}_{\gamma}) - \alpha E(\text{Fe}) - \beta E(\text{Co}) - \gamma E(\text{N}). \quad (1)$$

Here, $E(Fe_{\alpha}Co_{\beta}N_{\gamma})$ is the total energy per atom of an $Fe_{\alpha}Co_{\beta}N_{\gamma}$ structure. Reference energies are the total energies per atom of bcc Fe, hcp Co, and solid nitrogen (α -N₂), denoted as E(Fe), E(Co), and E(N), respectively. In Table I, we list the lattice parameters and Wyckoff positions of these phases. Structures with a negative formation energy are likely to be stable against decomposition into elemental phases. The formation energy for nitrides would be sensitive to the choice of the reference nitrogen energy. Various correction schemes, especially for nitrides exhibiting semiconducting or insulating characteristics, have been pursued by researchers including the fitted elemental reference energies scheme and a gas-fit reference scheme [47–50]. Here, we use as reference

TABLE I. Space group, lattice constants (a and c), and Wyckoff positions of elemental phases of Fe, Co, and N. These structural parameters are used for calculating the reference energies in Eq. (1).

	Space group [Number]	Structural parameters			
Material		a (Å)	c (Å)	Wyckoff positions	
bcc Fe hcp Co α-N ₂	Im3m [229] P6 ₃ /mmc [194] Pa3 [205]	2.866 2.510 5.856	4.071	2a (0, 0, 0) $2c (1/3, 2/3, 1/4)$ $8c (u, u, u)$ $u = 0.054869$	

the energy of α -N₂, which is the stable state retrieved from the "Phase Diagram" app of the Materials Project [51,52].

C. Magnetic anisotropy energy

For each structure, we calculate the total energy for magnetic moments oriented along the Cartesian (100), (010), and (001) directions, respectively. The direction associated with the lowest total energy can be labeled as the magnetic "easy" direction. The direction for the second lowest total energy can also be labeled as the magnetic "intermediate" direction. The magnetic anisotropy energy (MAE) can be expressed as the total-energy difference between ferromagnetic states with different magnetization directions:

$$E^{\rm MAE} = E_{\rm intermediate} - E_{\rm easy}. \tag{2}$$

The spins of all atoms are pointing in the same direction (ferromagnetic) during the MAE calculation. The magnetocrystalline anisotropy constant K_1 is obtained by dividing the MAE, $E^{\rm MAE}$, by the volume of the unit cell, V:

$$K_1 = E^{\text{MAE}}/V. (3)$$

D. Spatial decomposition of MAE

Within second-order perturbation theory [53,54], the MAE can be decomposed into contributions from individual sites in the unit cell. We adopt the spatial decomposition scheme of Antropov and co-workers [53,54], where we express the MAE as a half of the sum of the local MAEs over all atomic sites in the unit cell:

$$E^{\text{MAE-sum}} = \frac{1}{2} \sum_{i} E^{\text{MAE-SO}}(i)$$

$$= \frac{1}{2} \sum_{i} \left\{ E_{\text{intermediate}}^{\text{SO}}(i) - E_{\text{easy}}^{\text{SO}}(i) \right\}. \tag{4}$$

In this scheme, the site-resolved MAE is defined as the difference in the spin-orbit (SO) coupling energy at site i between two magnetization orientations:

$$E^{\text{MAE-SO}}(i) = E_{\text{intermediate}}^{\text{SO}}(i) - E_{\text{easy}}^{\text{SO}}(i). \tag{5}$$

The subscript indicates the direction of the local magnetic moments. This MAE decomposition scheme was carefully tested for $L1_0$ -ordered binary alloys and the α'' phase of Fe₁₆N₂ [53,54].

E. Machine learning

Machine-learning models for predicting relationships between chemical compositions, crystal structures, their formation energies, and magnetic properties (e.g., magnetic moments) can play an important role in accelerating material discovery. Our ML approach adopts a crystal graphic convolutional neural network (CGCNN) ML model [55] trained by our ab initio calculations. Our model learns material properties directly from both atomic information and bonding interactions between atoms, providing a universal and interpretable representation of crystalline materials. Crystal graphs are constructed with the nodes representing atoms and the edges representing connections between atoms in a crystal. The atomic feature vector includes the group number, the period number, electronegativity, covalent radius, number of valence electrons, first ionization energy, electron affinity, block (i.e., s, p, d, and f), and atomic volume. The bond feature vector includes the atom distance. Continuous properties such as the electronegativity are discretized into ten categories. (See the supplemental material of Ref. [55] for the range of each property). A convolutional neural network is built on top of the crystal graph to construct the proper descriptors that are optimal for predicting target properties. This method has been proven to provide reliable estimation of DFT calculated materials properties (such as formation energies, band gap, and bulk moduli) with good accuracy and computational efficiency.

We train a CGCNN model using our *ab initio* DFT results. Crystallographic data are stored in a standard crystallographic information file [56], and targeted properties are prepared as input data. The input data were randomly divided into training, validation, and test sets. The best-performing model that provides the lowest mean absolute error for the validation set is selected from 30 epochs during the computation. The number of epochs is set to 30, which is big enough for each ML prediction to be converged to minimum error. We optimized all the parameters in the CGCNN framework, such as the batch size and the number of convolutional layers. Both macroscopic and site-specific magnetic properties are investigated in this paper. Macroscopic properties include the total magnetic moment and the magnetic anisotropy energy of each structure.

Site-specific properties can vary from site to site owing to the difference in local environments. Inspired by the idea that site-specific properties are dominated by the nearest-neighbor atoms, we propose a universal approach for ML prediction of site-specific properties. In the first step, we select the atom of interest and all its nearest neighbors to generate a "cluster" centered on this specific atom. In the next step, the cluster is placed in a large cell with periodic boundary conditions to convert the cluster into a "crystal" for CGCNN. The cell is chosen to be large enough to avoid interactions among the atoms in different clusters due to the periodicity. For a given crystal structure, such a site-specific cluster and cell geometry can be generated for each nonequivalent site in the original crystal. The properties associated with the atom at the center of the clusters are used as the target values for ML training and prediction. All the ML parameters are reoptimized within this approach. We utilize this approach to predict the site-specific magnetic moment and the spin-orbit coupling energy.

TABLE II. Numbers by crystal system of Fe-N, Co-N, Fe-Co, and Fe-Co-N compounds examined in this paper. Crystallographic data of these compounds are taken from the Materials Project [34] and the Magnetic Materials Database [32].

Crystal system	Fe-N	Co-N	Fe-Co	Fe-Co-N	Total
Triclinic	0	12	0	8	20
Monoclinic	1	41	0	17	59
Orthorhombic	10	69	1	100	180
Tetragonal	6	16	5	112	139
Trigonal	7	8	0	1	16
Hexagonal	4	7	0	1	12
Cubic	0	18	5	3	26
Total	28	171	11	242	452

III. CRYSTAL STRUCTURES

We employed the Materials Project [34] and the Magnetic Materials Database [32] to collect Fe-Co-N structures. The Magnetic Materials Database provides several hundred Fe-rich compounds. These compounds include stable and metastable structures discovered through crystal structure searches using adaptive genetic algorithms [57,58]. Table II shows the numbers of the collected structures by crystal system. The collected structures include ternary Fe-Co-N compounds and binary compounds, such as Fe-N. Crystallographic data are analyzed using the PYMATGEN library [59].

Our calculations were carried out on all the 452 $Fe_{\alpha}Co_{\beta}N_{\gamma}$ structures. We did not use the properties listed in the Materials Project such as the total energy and total magnetic moment since we specified a different energy cutoff. Additionally, we calculated the site-specific properties. Only the crystallographic structure information from the two databases is used in this paper. All other data are calculated from our present work.

IV. RESULTS AND DISCUSSION

A. Phase diagram

We carried out high-throughput DFT spin-polarized calculations to compute the formation energies for the collected $Fe_{\alpha}Co_{\beta}N_{\gamma}$ structures. We examined the structural stability of each compound by composing a phase diagram, where we plot the calculated formation energies as a function of chemical composition.

Figure 1(a) shows the phase diagram obtained for Fe-N compounds. Our calculations using a GGA functional yield the formation energy to be negative for not only experimentally known phases but also some metastable Fe-N phases. The former group consists of FeN, a nonmagnetic phase with a cubic unit cell, and Fe₃N, a ferromagnetic phase (6.2 μ_B/f .u.) with a space group of $P6_322$. The latter group includes Fe₂N (trigonal $P\overline{3}1m$ and orthorhombic $P2_12_12$) and Fe₁₂N₅ ($P\overline{3}1m$).

Figure 1(b) shows the phase diagram obtained for Co-N compounds. The formation energy is predicted to be positive for all the Co-N structures. Our GGA results are consistent with previous work [14]. We find that CoN, an experimental phase with space group of $F\overline{4}3m$, has a formation

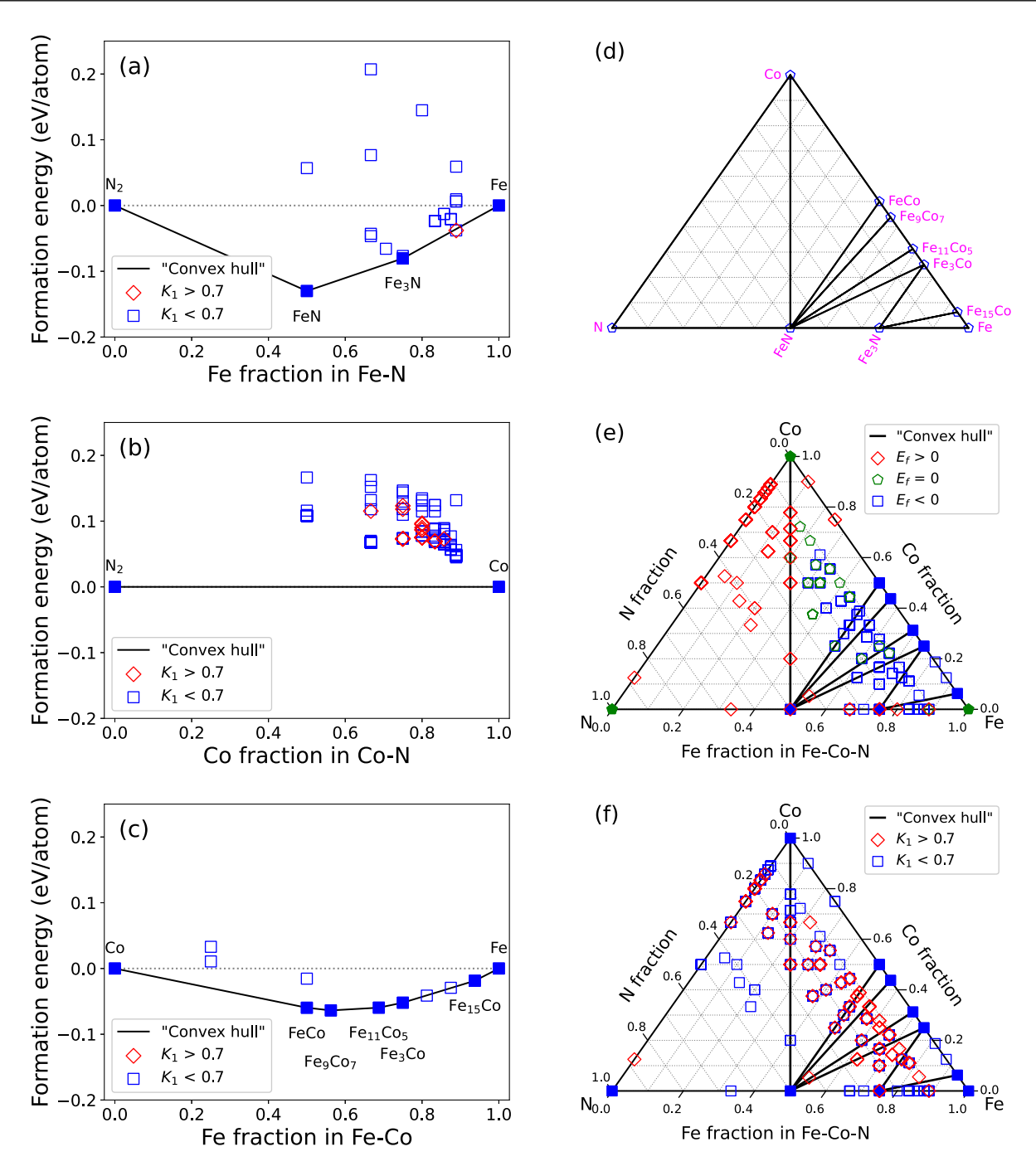


FIG. 1. Phase diagrams of (a) Fe-N, (b) Co-N, and (c) Fe-Co compounds. Stable phases are shown as filled symbols. The solid lines represent the lower limit in formation energy, called the "convex hull." Here, structures are classified by the magnitude of the magnetic anisotropy constant K_1 . (d) For a ternary system, the convex hull can be shown as a two-dimensional projection. Phase diagrams of an Fe-Co-N system for (e) the formation energy E_f and (f) K_1 .

energy of 0.11 eV/atom relative to the convex hull. As shown in Fig. 1(b), many metastable Co-rich phases have formation energies comparable to or lower than that of CoN, indicating the possibility of these low-energy structures being produced.

Figure 1(c) shows the phase diagram obtained for Fe-Co compounds. We find several Fe-Co phases that are distributed in the vicinity of the convex hull (within \sim 0.1 eV/atom relative to the hull). Such metastable phases include FeCo with *Cmmm* and FeCo₃ with *P*4/*mmm* and *Pm* $\overline{3}m$.

Figure 1(d) shows the convex hull of an Fe-Co-N system as a two-dimensional projection. In Fig. 1(e), we show the ternary phase diagram with respect to the formation energies of Fe-Co-N compounds. From our calculations, 242 structures are predicted to have a negative formation energy, being less likely to decompose into elemental phases. Most of these structures have a formation energy of less than 100 meV/atom relative to the convex hull. Metastable structures in such an energy range often correspond to an accessible phase in experiment, as discussed elsewhere [32].

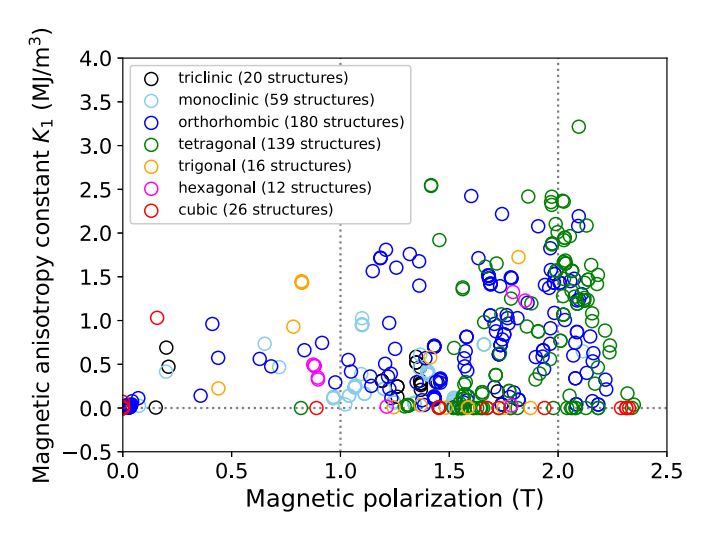


FIG. 2. Magnetic anisotropy constant K_1 and magnetic polarization for a total of 452 Fe_{α}Co_{β}N_{γ} crystal structures.

B. Magnetic anisotropy energy

We compute the magnetic anisotropy energy using a totalenergy difference scheme [i.e., using Eqs. (2) and (3)] in our DFT spin-orbit calculations. In Figs. 1(a)–1(d), we show the magnitude of K_1 of each structure by using different colors and symbols. Our calculations yield a sizable K_1 for many metastable structures with an Fe-rich or Co-rich composition. However, most of the stable $Fe_{\alpha}Co_{\beta}N_{\gamma}$ phases yield $K_1=0$. This low value arises from the cubic symmetry or a nonmagnetic ground state in these structures.

Figure 2 shows the distribution of K_1 with different crystal systems. We find 34 Fe-Co-N structures (out of 452 structures we examined) with a strong magnetic anisotropy, i.e., a K_1 value of more than 2 MJ/m³. Among these there are 11 orthorhombic and 21 tetragonal structures. Owing to an Fe-rich or Co-rich stoichiometry, these large-MAE structures possess high magnetic polarization as large as 1–2.1 T.

C. Spatial decomposition of MAE

We calculate the spin-orbit coupling energies at each atomic site of all the structures. This is done for each of the three Cartesian axes as a spin-quantization axis. In addition to the calculated site-specific spin-orbit coupling energies, we derive the local MAEs for individual sites using Eq. (5). We sum up the site-specific MAEs over all sites in the unit cell [Eq. (4)] to estimate the total MAE for each structure. The total MAEs from Eq. (4) are directly compared with those from Eq. (2).

Figure 3 shows our results for the spatial decomposition of the MAEs for Fe-N, Co-N, Fe-Co, and Fe-Co-N structures. In Fig. 3, we plot the total MAEs derived from the site-specific MAEs against the ones derived from the total-energy difference scheme. Our MAE data sets strongly correlate with each other with a linear relationship. The spatial decomposition scheme using Eq. (4) works well for all the structures over a large span of K_1 from 0 to 2.7 meV/f.u. This energy range corresponds to a range from 0 to 3.2 MJ/m³. We find that our spatial decomposition scheme underestimates the MAE. This

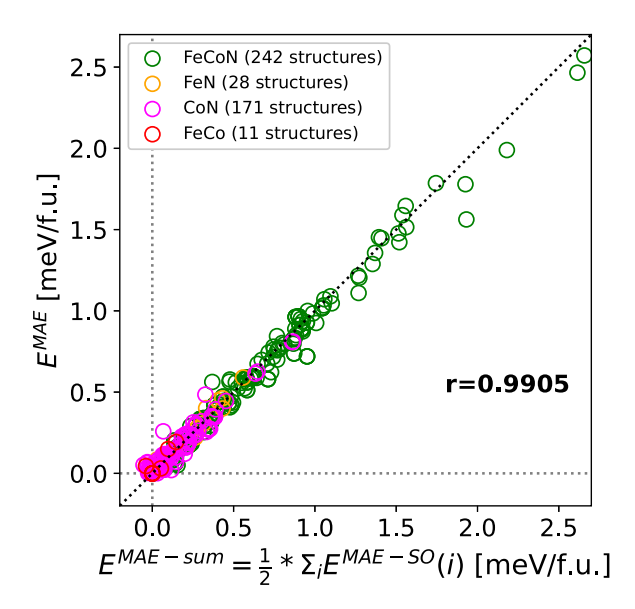


FIG. 3. Comparison of two methods for calculating the magnetic anisotropy energy. MAE values derived from the total-energy difference scheme [Eq. (2)] are on the vertical axis, while those derived from a spatial decomposition scheme (total MAE as a half of the sum of site-specific MAEs over all atomic sites) [Eq. (4)] are on the horizontal axis. The Pearson's correlation coefficient, denoted as r, is given as a measure of correlation between the two data sets. The data points on the dotted line with a slope of unity indicate that the predicted data perfectly fit the reference data.

is partly due to higher-order terms, which are omitted in the present formalism for decomposing the total MAE.

We introduce the coefficient of determination, denoted R^2 , as a measure of correlation between the two data sets. The R^2 coefficient is calculated by

$$R^{2} = 1 - \frac{\sum (E^{\text{MAE}} - E^{\text{MAE-sum}})^{2}}{\sum (E^{\text{MAE}} - \langle E^{\text{MAE}} \rangle)^{2}}.$$
 (6)

 $\langle E^{\rm MAE} \rangle$ denotes the mean of the MAE data. The summation runs over all structures. The R^2 coefficient can range from 0 to 1. A value of 1 means that the predicted values are identical to the reference values. The closer it is to 1, the stronger the positive linear relationship between the two data sets.

We find that the calculated R^2 value is close to unity, as listed in Table III. Our results indicate that the spatial decomposition scheme of Eq. (4) is an effective way of splitting the total MAE into site-specific components. We quantify the performance of the MAE decomposition scheme from a different perspective. We calculate the Pearson's product-

TABLE III. Cross-validation scores and correlation coefficients between two sets of MAE data. Reference MAE data are derived from the total-energy difference scheme, while estimated MAE data are obtained from the spatial decomposition scheme.

Measure	Value for K_1
Coefficient of determination [Eq. (6)] Pearson's correlation coefficient [Eq. (7)]	$R^2 = 0.9804$ $r = 0.9905$

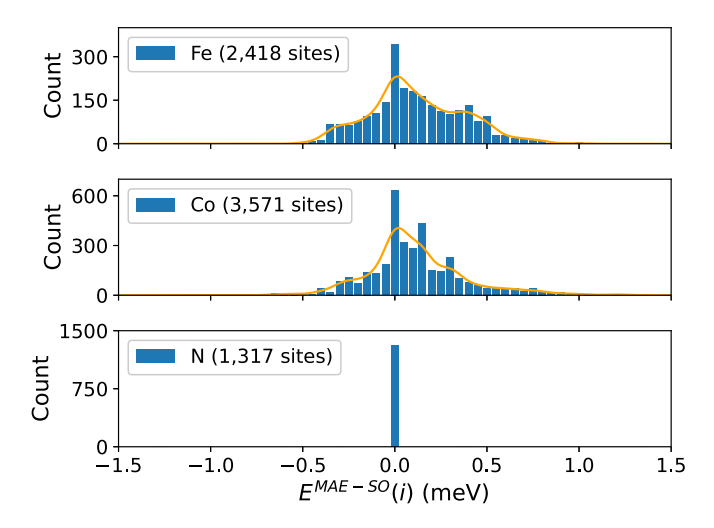


FIG. 4. Distribution of the site-specific magnetic anisotropy energies, $E^{\rm MAE-SO}(i)=E^{\rm SO}_{\rm intermediate}(i)-E^{\rm SO}_{\rm easy}(i)$, obtained from our first-principles calculations. The subscript indicates the quantization axis for spins and i denotes the site index. A total of 452 ${\rm Fe}_{\alpha}{\rm Co}_{\beta}{\rm N}_{\gamma}$ structures is used. The total number of atomic sites for each element is given in the legend. A fitting curve with a Gaussian distribution is also shown.

moment correlation coefficient as

$$r = \frac{\sum (X - \langle X \rangle)(Y - \langle Y \rangle)}{\sqrt{\sum (X - \langle X \rangle)^2 \sum (Y - \langle Y \rangle)^2}},$$
 (7)

where $X = E^{\rm MAE}$ and $Y = E^{\rm MAE-sum}$. The correlation coefficient r can take a value from +1 (a perfect positive correlation) to -1 (a perfect negative correlation). For the two sets of our MAE data, the r value is 0.99. This means that the two MAE data sets are highly correlated.

D. Site-specific MAE

We compile all of the calculated site-specific MAEs into a single data file. In particular, we associate site-specific MAE data with atomic structure data, such as species on each site and fractional coordinates of each species. A one-to-one relationship between MAE data and structure data is essential to analyze the site-specific MAEs. Such a data set is also useful to construct a machine-learning model, as we will illustrate in the following.

In Fig. 4, we show the distribution of site-specific MAEs for each species. Overall, many Fe and Co sites possess a local MAE of the order of several tenths of a meV. The calculated site-specific MAEs range from -0.5 to 0.5 meV. This is because the sign and magnitude of the local MAEs vary from site to site, indicating the influence of bonding configurations on a local MAE. An atomic MAE at a nitrogen site is negligibly small owing to the very weak spin-orbit couplings of nitrogen.

E. Machine learning for magnetic properties

The performance of ML-based prediction often relies on the size of sample data (known as "training data") in database space. Here, we illustrate the importance and utility of site-specific data for ML modeling. In particular, we show that thousands of microscopic data, such as the site-specific spin-orbit energies and the local magnetic moments associated with local atomic structures, can serve as good training data for constructing a ML model to predict the MAE and magnetization of new materials. Our ML-based approach will lead to efficient computational screening for the design of new magnets.

We illustrate the feasibility of our CGCNN ML model approach for predicting the magnetic properties of new Fe-Co-N structures. For the total magnetic moment and the magnetic anisotropy energy, we use the data for a total of 452 structures. ML models are trained with 80% of the data and then validated with 10% of the data. The remaining 10% of the data are used as a test set.

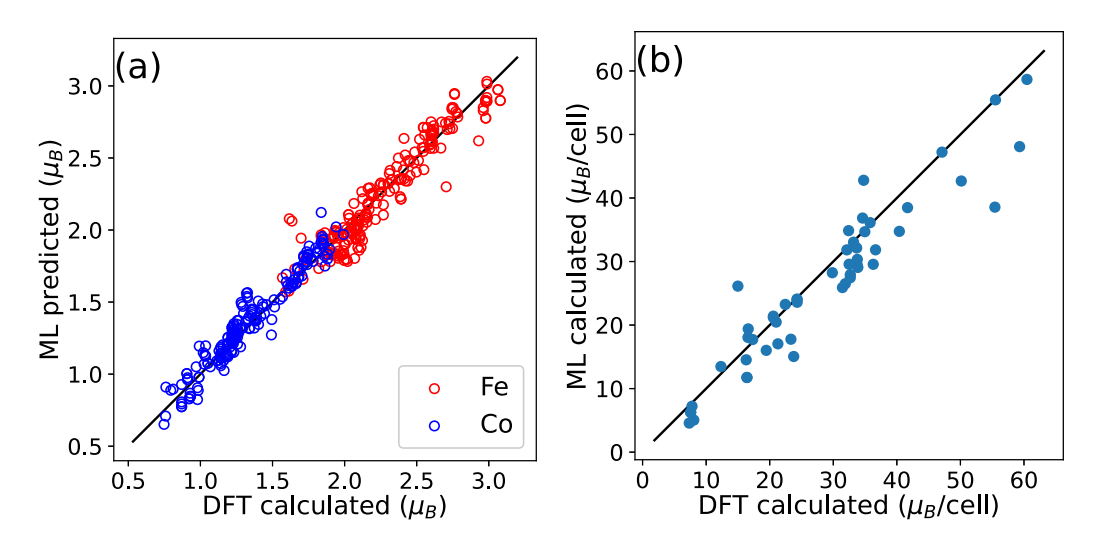


FIG. 5. (a) The site-specific magnetic moment and (b) the total magnetic moment per unit cell for Fe-Co-N compounds. Magnetic moment values from first-principles DFT calculations are on the horizontal axis, while those predicted from our ML model are on the vertical axis. Data points on the solid line (with a slope of unity) indicate a perfect fit between the ML-predicted and DFT-predicted data.

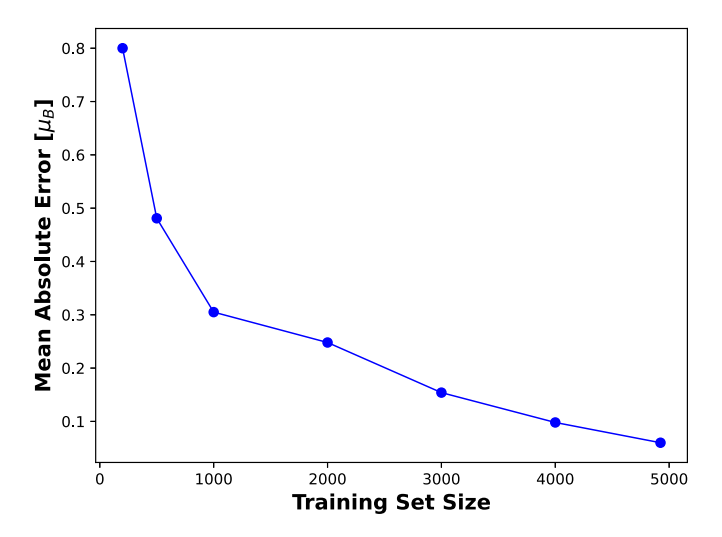


FIG. 6. The mean absolute error vs the size of training set data for the site-specific magnetic moment prediction.

We also study site-specific magnetic moments and the atomic spin-orbit coupling energies using our method. A total of 4924 "clusters" are generated from the original 452 Fe-Co-N crystal structures. Each cluster can be associated with the site-specific magnetic properties corresponding to the atom centered on a cluster. (Due to difficulties in the convergence of some calculations, the number of data for the spin-orbit energies was 4790, which was less than that for the local magnetic moments, 4924). The data set is divided into training, validation, and test data sets with the same 8:1:1 ratio.

In Figs. 5(a) and 5(b), we plot the results for the magnetic moments predicted by our CGCNN ML model. The ML results are compared with the DFT calculated results. The total and site-specific magnetic moments from our ML prediction agree very well with DFT calculations. For site-specific magnetic moments, we get a small mean absolute error of 0.055 μ_B . In Fig. 5(a), almost all the data points lie in the vicinity of the perfect-fit line (with a slope of unity),

indicating that our CGCNN-based approach works very well for predicting the site-specific magnetic moments. The scaling of the accuracy against the size of training data is plotted in Fig. 6. We estimate that the error will fall below 0.1 μ_B per site when the training set has a size of 4000. Our CGCNN model also works well for the total magnetic moment. As shown in Fig. 5(b), the data points are scattered around the 45° line. It shows a good agreement between the DFT and ML results. The root-mean-square error is about 2.8 μ_B per unit cell.

We illustrate the capability of our CGCNN ML model to describe the magnetic anisotropy energy. Figure 7(a) shows the result for the site-specific magnetic anisotropy energies. The data points are distributed along the 45° reference line, with a mean absolute error of 0.15 meV per atomic site. Our ML model enables us to estimate the total magnetic anisotropy energies as shown in Fig. 7(b). We find a mean absolute error of 0.5 MJ/m³ for the total MAE. The model is the most accurate when the training data set covers a large range of values.

The computational time required for ML predictions is much faster compared with that of DFT calculations. A single run for the total magnetic moment and the magnetic anisotropy energy of 452 structures takes 5 min to complete on a computational node with 16 cores. Suppose we perform DFT calculations for all of these 452 structures, which includes the collinear calculation and the spin-orbit calculations with magnetic moments aligned along three different directions. The computational time for this task is 79 days on a 64-core Intel Knights Landing (KNL) node. For site-specific magnetic properties, our ML calculation takes about 30 min to finish for all of the 4790 atomic sites.

V. SUMMARY

We present a promising machine-learning model focusing on site magnetic properties for rapid screening in materials design. We analyzed the magnetic anisotropy energy of

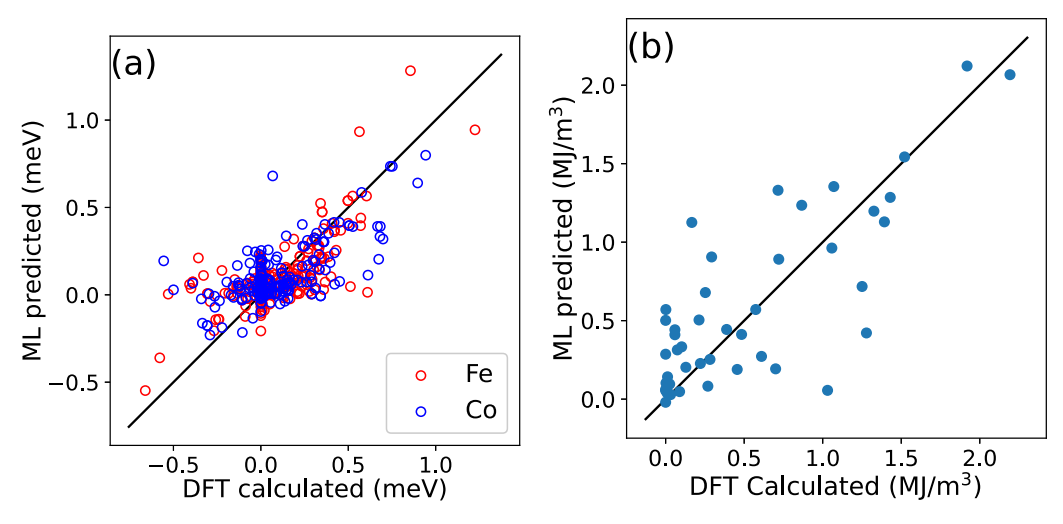


FIG. 7. (a) The site-specific MAE, $E^{\text{MAE-SO}}$, in units of meV and (b) the total MAE divided by volume, K_1 , in units of MJ/m³ for Fe-Co-N compounds. MAE values from first-principles DFT calculations are on the horizontal axis, while those predicted from our ML model are on the vertical axis. Data points on the solid line (with a slope of unity) indicate a perfect fit between the ML-predicted and DFT-computed data.

iron-cobalt nitrides using high-throughput first-principles calculations and ML models. The spatial decomposition scheme we employed works well for a wide range of magnetic anisotropy energy. The CGCNN ML model trained with structural details on each atomic site has great potential to reproduce the site-specific spin-orbit coupling energies. The CGCNN ML approach is applied to predicting the site-specific magnetic moments as well as the total magnetic moments. Our results indicate the capability of our ML-assisted approach to accelerate computational screening of candidate materials with high magnetization and a large magnetic anisotropy energy.

Crystallographic and computational data, such as the formation energy and magnetic anisotropy constants, for the iron-cobalt nitrides are available from the Magnetic Materials Database [32].

ACKNOWLEDGMENTS

This research is supported by the U.S. National Science Foundation (NSF) through the Designing Materials to Revolutionize and Engineer our Future (DMREF) program with Awards No. 1729202 and No. 1729677. High-performance computing resources were provided by the Texas Advanced Computing Center (TACC), through the Extreme Science and Engineering Discovery Environment (XSEDE) allocation. Work at Guangdong University of Technology (GDUT) was supported by the Guangdong Basic and Applied Basic Research Foundation (Grant No. 2021A1515110328). R.W. also thanks the Center of Campus Network & Modern Educational Technology of GDUT for providing computational resources and technical support for this work. C.Z. was supported by the National Natural Science Foundation of China (Grants No. 11874318 and No. 11774299).

- [1] S. Chikazumi, *Physics of Ferromagnetism*, 2nd ed., International Series of Monographs on Physics (Oxford University Press, Oxford, 2009).
- [2] J. M. D. Coey, Magnetism and Magnetic Materials (Cambridge University Press, Cambridge, 2010).
- [3] R. Skomski and J. M. D. Coey, Magnetic anisotropy how much is enough for a permanent magnet?, Scr. Mater. 112, 3 (2016).
- [4] B. Balasubramanian, P. Manchanda, R. Pahari, Z. Chen, W. Zhang, S. R. Valloppilly, X. Li, A. Sarella, L. Yue, A. Ullah, P. Dev, D. A. Muller, R. Skomski, G. C. Hadjipanayis, and D. J. Sellmyer, Chiral Magnetism and High-Temperature Skyrmions in B20-Ordered Co-Si, Phys. Rev. Lett. 124, 057201 (2020).
- [5] J. F. Herbst, R₂Fe₁₄B materials: Intrinsic properties and technological aspects, Rev. Mod. Phys. 63, 819 (1991).
- [6] K. J. Strnat and R. M. Strnat, Rare earth-cobalt permanent magnets, J. Magn. Magn. Mater. 100, 38 (1991).
- [7] D. Weller and T. McDaniel, Media for extremely high density recording, in *Advanced Magnetic Nanostructures*, edited by D. Sellmyer and R. Skomski (Springer, Boston, MA, 2006), pp. 295–324.
- [8] C. Tannous and R. L. Comstock, Magnetic information-storage materials, in *Springer Handbook of Electronic and Photonic Materials*, edited by S. Kasap and P. Capper (Springer, Cham, Switzerland, 2017), pp. 1185–1223.
- [9] G. B. Haxel, J. B. Hedrick, and G. J. Orris, Rare earth elements– critical resources for high technology, U.S. Geological Survey, Fact Sheet 087-02 (2002).
- [10] Materials Genome Initiative Strategic Plan, http://www.nist. gov/mgi/upload/MGI-StrategicPlan-2014.pdf.
- [11] J. Cui, M. Kramer, L. Zhou, F. Liu, A. Gabay, G. Hadjipanayis, B. Balasubramanian, and D. Sellmyer, Current progress and future challenges in rare-earth-free permanent magnets, Acta Mater. 158, 118 (2018).
- [12] B. Balasubramanian, M. Sakurai, C.-Z. Wang, X. Xu, K.-M. Ho, J. R. Chelikowsky, and D. J. Sellmyer, Synergistic computational and experimental discovery of novel magnetic materials, Mol. Syst. Des. Eng. 5, 1098 (2020).

- [13] X. Zhao, C.-Z. Wang, Y. Yao, and K.-M. Ho, Large magnetic anisotropy predicted for rare-earth-free Fe_{16-x}Co_xN₂ alloys, Phys. Rev. B **94**, 224424 (2016).
- [14] X. Zhao, L. Ke, C.-Z. Wang, and K.-M. Ho, Metastable cobalt nitride structures with high magnetic anisotropy for rare-earth free magnets, Phys. Chem. Chem. Phys. **18**, 31680 (2016).
- [15] J. Zhang, M. C. Nguyen, B. Balasubramanian, B. Das, D. J. Sellmyer, Z. Zeng, K.-M. Ho, and C.-Z. Wang, Crystal structure and magnetic properties of new Fe₃Co₃ X_2 (X = Ti, Nb) intermetallic compounds, J. Phys. D: Appl. Phys. **49**, 175002 (2016).
- [16] S. Q. Wu, B. Balamurugan, X. Zhao, S. Yu, M. C. Nguyen, Y. Sun, S. R. Valloppilly, D. J. Sellmyer, K. M. Ho, and C. Z. Wang, Exploring new phases of Fe_{3-x}Co_xC for rare-earth-free magnets, J. Phys. D: Appl. Phys. 50, 215005 (2017).
- [17] S. Yu, X. Zhao, S. Wu, M. C. Nguyen, Z.-z. Zhu, C.-Z. Wang, and K.-M. Ho, New structures of Fe₃S for rare-earth-free permanent magnets, J. Phys. D: Appl. Phys. 51, 075001 (2018).
- [18] M. Sakurai, X. Zhao, C.-Z. Wang, K.-M. Ho, and J. R. Chelikowsky, Influence of nitrogen dopants on the magnetization of Co₃N clusters, Phys. Rev. Materials **2**, 024401 (2018).
- [19] M. Sakurai and J. R. Chelikowsky, Enhanced magnetic moments in Mn-doped FeCo clusters owing to ferromagnetic surface Mn atoms, Phys. Rev. Materials 3, 044402 (2019).
- [20] B. Balamurugan, B. Das, W. Y. Zhang, R. Skomski, and D. J. Sellmyer, Hf–Co and Zr–Co alloys for rare-earth-free permanent magnets, J. Phys.: Condens. Matter 26, 064204 (2014).
- [21] X. Zhao, M. C. Nguyen, W. Y. Zhang, C. Z. Wang, M. J. Kramer, D. J. Sellmyer, X. Z. Li, F. Zhang, L. Q. Ke, V. P. Antropov, and K. M. Ho, Exploring the Structural Complexity of Intermetallic Compounds by an Adaptive Genetic Algorithm, Phys. Rev. Lett. 112, 045502 (2014).
- [22] X. Zhao, L. Ke, M. C. Nguyen, C.-Z. Wang, and K.-M. Ho, Structures and magnetic properties of Co-Zr-B magnets studied by first-principles calculations, J. Appl. Phys. (Melville, NY) 117, 243902 (2015).
- [23] M. Sakurai, S. Wu, X. Zhao, M. C. Nguyen, C.-Z. Wang, K.-M. Ho, and J. R. Chelikowsky, Magnetocrystalline anisotropy in

- YCo₅ and ZrCo₅ compounds from first-principles real-space pseudopotentials calculations, Phys. Rev. Materials **2**, 084410 (2018).
- [24] Y. Saad, D. Gao, T. Ngo, S. Bobbitt, J. R. Chelikowsky, and W. Andreoni, Data mining for materials: Computational experiments with *AB* compounds, *Phys. Rev. B* **85**, 104104 (2012).
- [25] S. Ubaru, A. Miedlar, Y. Saad, and J. R. Chelikowsky, Formation enthalpies for transition metal alloys using machine learning, Phys. Rev. B 95, 214102 (2017).
- [26] K. T. Butler, D. W. Davies, H. Cartwright, O. Isayev, and A. Walsh, Machine learning for molecular and materials science, Nature (London) 559, 547 (2018).
- [27] J. E. Gubernatis and T. Lookman, Machine learning in materials design and discovery: Examples from the present and suggestions for the future, Phys. Rev. Materials 2, 120301 (2018).
- [28] G. Carleo, I. Cirac, K. Cranmer, L. Daudet, M. Schuld, N. Tishby, L. Vogt-Maranto, and L. Zdeborová, Machine learning and the physical sciences, Rev. Mod. Phys. 91, 045002 (2019).
- [29] S. Sanvito, C. Oses, J. Xue, A. Tiwari, M. Zic, T. Archer, P. Tozman, M. Venkatesan, M. Coey, and S. Curtarolo, Accelerated discovery of new magnets in the Heusler alloy family, Sci. Adv. 3, e1602241 (2017).
- [30] J. Nelson and S. Sanvito, Predicting the Curie temperature of ferromagnets using machine learning, Phys. Rev. Materials 3, 104405 (2019).
- [31] S. Curtarolo, W. Setyawan, G. L. Hart, M. Jahnatek, R. V. Chepulskii, R. H. Taylor, S. Wang, J. Xue, K. Yang, O. Levy, M. J. Mehl, H. T. Stokes, D. O. Demchenko, and D. Morgan, AFLOW: An automatic framework for high-throughput materials discovery, Comput. Mater. Sci. 58, 218 (2012).
- [32] M. Sakurai, R. Wang, T. Liao, C. Zhang, H. Sun, Y. Sun, H. Wang, X. Zhao, S. Wang, B. Balasubramanian, X. Xu, D. J. Sellmyer, V. Antropov, J. Zhang, C.-Z. Wang, K.-M. Ho, and J. R. Chelikowsky, Discovering rare-earth-free magnetic materials through the development of a database, Phys. Rev. Materials 4, 114408 (2020).
- [33] L. Talirz, S. Kumbhar, E. Passaro, A. V. Yakutovich, V. Granata, F. Gargiulo, M. Borelli, M. Uhrin, S. P. Huber, S. Zoupanos, C. S. Adorf, C. W. Andersen, O. Schütt, C. A. Pignedoli, D. Passerone, J. Vande Vondele, T. C. Schulthess, B. Smit, G. Pizzi, and N. Marzari, Materials cloud, a platform for open computational science, Sci. Data 7, 299 (2020).
- [34] A. Jain, S. P. Ong, G. Hautier, W. Chen, W. D. Richards, S. Dacek, S. Cholia, D. Gunter, D. Skinner, G. Ceder, and K. A. Persson, Commentary: The Materials Project: A materials genome approach to accelerating materials innovation, APL Mater. 1, 011002 (2013).
- [35] C. Draxl and M. Scheffler, The NOMAD laboratory: From data sharing to artificial intelligence, J. Phys. Mater. 2, 036001 (2019).
- [36] J. E. Saal, S. Kirklin, M. Aykol, B. Meredig, and C. Wolverton, Materials design and discovery with high-throughput density functional theory: The open quantum materials database (OQMD), JOM 65, 1501 (2013).
- [37] J. Hill, G. Mulholland, K. Persson, R. Seshadri, C. Wolverton, and B. Meredig, Materials science with large-scale data and informatics: Unlocking new opportunities, MRS Bull. 41, 399 (2016).
- [38] P. Hohenberg and W. Kohn, Inhomogeneous electron gas, Phys. Rev. 136, B864 (1964).

- [39] W. Kohn and L. J. Sham, Self-consistent equations including exchange and correlation effects, Phys. Rev. **140**, A1133 (1965).
- [40] J. P. Perdew, K. Burke, and M. Ernzerhof, Generalized Gradient Approximation Made Simple, Phys. Rev. Lett. 77, 3865 (1996).
- [41] P. E. Blöchl, Projector augmented-wave method, Phys. Rev. B 50, 17953 (1994).
- [42] H. J. Monkhorst and J. D. Pack, Special points for Brillouinzone integrations, Phys. Rev. B 13, 5188 (1976).
- [43] M. Sakurai and J. R. Chelikowsky, Real-space pseudopotential method for calculating magnetocrystalline anisotropy, Phys. Rev. Materials 2, 084411 (2018).
- [44] G. Kresse and J. Furthmüller, Efficiency of ab-initio total energy calculations for metals and semiconductors using a plane-wave basis set, Comput. Mater. Sci. 6, 15 (1996).
- [45] G. Kresse and J. Furthmüller, Efficient iterative schemes for ab initio total-energy calculations using a plane-wave basis set, Phys. Rev. B **54**, 11169 (1996).
- [46] S. Steiner, S. Khmelevskyi, M. Marsmann, and G. Kresse, Calculation of the magnetic anisotropy with projected-augmented-wave methodology and the case study of disordered Fe_{1-x}Co_x alloys, Phys. Rev. B 93, 224425 (2016).
- [47] W. Sun, A. Holder, B. Orvañanos, E. Arca, A. Zakutayev, S. Lany, and G. Ceder, Thermodynamic routes to novel metastable nitrogen-rich nitrides, Chem. Mater. 29, 6936 (2017).
- [48] V. Stevanović, S. Lany, X. Zhang, and A. Zunger, Correcting density functional theory for accurate predictions of compound enthalpies of formation: Fitted elemental-phase reference energies, Phys. Rev. B 85, 115104 (2012).
- [49] S. Lany, Semiconductor thermochemistry in density functional calculations, Phys. Rev. B 78, 245207 (2008).
- [50] L. Wang, T. Maxisch, and G. Ceder, A first-principles approach to studying the thermal stability of oxide cathode materials, Chem. Mater. **19**, 543 (2006).
- [51] S. P. Ong, L. Wang, B. Kang, and G. Ceder, Li-Fe-P-O₂ phase diagram from first principles calculations, Chem. Mater. 20, 1798 (2008).
- [52] S. P. Ong, A. Jain, G. Hautier, B. Kang, and G. Ceder, Thermal stabilities of delithiated olivine MPO₄ (M = Fe, Mn) cathodes investigated using first principles calculations, Electrochem. Commun. **12**, 427 (2010).
- [53] V. Antropov, L. Ke, and D. Åberg, Constituents of magnetic anisotropy and a screening of spin-orbit coupling in solids, Solid State Commun. 194, 35 (2014).
- [54] Y. Sun, Y.-X. Yao, M. C. Nguyen, C.-Z. Wang, K.-M. Ho, and V. Antropov, Spatial decomposition of magnetic anisotropy in magnets: Application to doped Fe₁₆N₂, Phys. Rev. B 102, 134429 (2020).
- [55] T. Xie and J. C. Grossman, Crystal Graph Convolutional Neural Networks for an Accurate and Interpretable Prediction of Material Properties, Phys. Rev. Lett. 120, 145301 (2018).
- [56] S. R. Hall, F. H. Allen, and I. D. Brown, The crystallographic information file (CIF): A new standard archive file for crystallography, Acta Crystallogr. Sect. A: Found. Crystallogr. 47, 655 (1991).
- [57] D. M. Deaven and K. M. Ho, Molecular Geometry Optimization with a Genetic Algorithm, Phys. Rev. Lett. **75**, 288 (1995).
- [58] S. Q. Wu, M. Ji, C. Z. Wang, M. C. Nguyen, X. Zhao, K. Umemoto, R. M. Wentzcovitch, and K. M. Ho, An adaptive

genetic algorithm for crystal structure prediction, J. Phys.: Condens. Matter **26**, 035402 (2013).

[59] S. P. Ong, W. D. Richards, A. Jain, G. Hautier, M. Kocher, S. Cholia, D. Gunter, V. L. Chevrier, K. A.

Persson, and G. Ceder, Python Materials ZGenomics (pymatgen): A robust, open-source python library for materials analysis, Comput. Mater. Sci. 68, 314 (2013).